

This is the Title of my Thesis

Johannes Bogen

December 2016

PROJECT THESIS  
Department of Physics  
Norwegian University of Science and Technology

Supervisor: Professor Antonius T. J. van Helvoort

## Preface

Here, you give a brief introduction to your work. What it is (e.g., a Master's thesis in RAMS at NTNU as part of the study program xxx and...), when it was carried out (e.g., during the autumn semester of 2021). If the project has been carried out for a company, you should mention this and also describe the cooperation with the company. You may also describe how the idea to the project was brought up.

You should also specify the assumed background of the readers of this report (who are you writing for).

Trondheim, 2012-12-16

(Your signature)

Ola Nordmann

## Acknowledgment

I would like to thank the following persons for their great help during ...

If the project has been carried out in cooperation with an external partner (e.g., a company), you should acknowledge the contribution and give thanks to the involved persons.

You should also acknowledge the contributions made by your supervisor(s).

O.N.

(Your initials)

## **Summary and Conclusions**

Here you give a summary of your work and your results. This is like a management summary and should be written in a clear and easy language, without many difficult terms and without abbreviations. Everything you present here must be treated in more detail in the main report. You should not give any references to the report in the summary – just explain what you have done and what you have found out. The Summary and Conclusions should be no more than two pages.

You may assume that you have got three minutes to present to the Rector of NTNU what you have done and what you have found out as part of your thesis. (He is an intelligent person, but does not know much about your field of expertise.)

# Contents

Preface . . . . .	i
Acknowledgment . . . . .	ii
Summary and Conclusions . . . . .	iii
<b>1 Introduction</b>	<b>2</b>
<b>2 Theory</b>	<b>4</b>
2.1 Semiconductor nanowires . . . . .	4
2.2 Transmission Electron Microscopy . . . . .	5
2.2.1 Electron emission . . . . .	5
2.2.2 Electron-sample interaction . . . . .	5
2.2.3 Scanning Transmission Electron Microscopy . . . . .	6
2.3 X-ray spectroscopy . . . . .	6
2.3.1 Energy-Dispersive X-Ray Spectroscopy (EDS) . . . . .	7
2.3.2 Quantitative X-ray Analysis . . . . .	8
2.3.3 Thickness estimation . . . . .	11
2.4 Electron diffraction . . . . .	12
2.4.1 Diffraction theory . . . . .	12
2.4.2 Electron diffraction in STEM . . . . .	14
2.4.3 Scanning Precession Electron Diffraction (SPED) . . .	14
2.5 Data analysis . . . . .	16
2.5.1 Template matching . . . . .	16
2.5.2 Re-binning and rotating multidimensional data . . . . .	16
<b>3 Experimental</b>	<b>19</b>
3.1 Equipment . . . . .	19
3.2 Material . . . . .	19
3.3 Dataset matching . . . . .	19

3.4	Quantitative analysis . . . . .	21
<b>4</b>	<b>Results</b>	<b>24</b>
4.1	Dataset matching . . . . .	24
4.2	Determination of $\zeta$ -values . . . . .	27
4.3	Quantification . . . . .	28
<b>5</b>	<b>Discussion</b>	<b>36</b>
5.1	Dataset matching . . . . .	36
5.1.1	Step 1 . . . . .	36
5.2	Determination of $\zeta$ -values . . . . .	39
5.3	Quantification . . . . .	40
5.4	Comparison to theory . . . . .	42
<b>A</b>	<b>Acronyms</b>	<b>44</b>
<b>B</b>	<b>Additional Information</b>	<b>45</b>
B.1	Introduction . . . . .	45
B.1.1	More Details . . . . .	45

# Chapter 1

## Introduction

Since their discovery in the late 1990's, semiconductor nanowires have been researched extensively as a potential new building block in the fields of electronics, opto-electronics, energy generation and storage. Devices such as batteries and solar cells are examples of devices in which semiconductor nanowires could make a great difference in peoples' everyday lives [1]. However, a deeper understanding of the nanoscale physics involved is required for this to become a reality [2]. Semiconductor nanowires are one of the most promising building-blocks in nanoscience. This is not only due to their small and excellent properties, but in particular because of the possibility to design them ab initio, from the bottom up [3].

In research it is important to be able to measure the electrical properties of the nanowire. To do so, an electrical contact has to be attached to the wire. Unfortunately, the interface between the contact and the nanowire forms a Schottky barrier. If the resistance of the nanowire is measured, the high resistance in the barrier will dominate and accurate measurements of the resistance in the nanowire are impossible [?]. The interface should ideally act as an ohmic conductor.

Many attempts were made in the 1980's and 90's to stack metals onto thin-films in order to produce ohmic contacts [4], and the results found then are now investigated for use on nanowires. For GaAs-films, one of the best solutions involved depositing layers of Pd, Ge and Au, and then annealing it [2]. This has been done, but did not result in an ohmic contact, although

the annealing has significantly improved the properties. To explain why, it is necessary to investigate the resulting phases in the nanowire-metal interface [?].

A transmission electron microscope can be used to study the structure and composition of a material through many different techniques. Two of these techniques are energy-dispersive X-ray spectroscopy and selected area diffraction. Spectroscopy can help determine the composition of the material, while diffraction is necessary for structural information. If used together, these two techniques can therefore provide complete information about the material. The purpose of this project has been two-folded. Due to having been collected at different microscopes, the diffraction data and the spectroscopy data is not aligned with each other. In order to study both signals simultaneously, the datasets have been scaled, rotated and translated in an attempt to match them pixel by pixel. The second part of the project has consisted of using the open-source Python library HyperSpy [5] to quantify the element compositions in select regions of interest on the annealed nanowire.

# Chapter 2

## Theory

### 2.1 Semiconductor nanowires

The basic semiconductor nanowire is a one-dimensional, uniform structure with a diameter typically in the range 3-500 nm [?]. Semiconductor nanowires are generally synthesized via the vapor-liquid-solid (VLS) process as illustrated in Fig. 2.1. In this process, a nanoparticles acting as a catalyst is heated above the eutectic point, creating a eutectic alloy. This takes place in the presence of the semiconductor-material in vapor-phase, which proceeds to be incorporated into the the alloy through the vapor/liquid-interface. The alloy will eventually supersaturate, after which further addition of the vapor causes the solid phase of the eutectic alloy to grow, creating a nanowire [3, 1].

When the nanowire is connected to a metal electrode, a Schottky barrier is usually formed in the interface. This barrier can hinder the flow of charge through the interface, which for many device applications is a necessity [2]. One way of overcoming this hindrance is by heavily doping the nanowire near the contact, enabling electrons to tunnel through the interface. The contact is often subsequently annealed to further improve the resistivity [3].

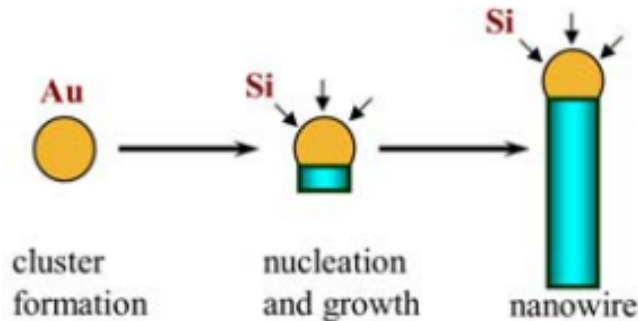


Figure 2.1: From [1]

## 2.2 Transmission Electron Microscopy

In a transmission electron microscope (TEM), a beam of electrons are transmitted onto a material. Compared to a microscope using visible light, an electron gives a much higher resolution due to the wavelength of electrons being much smaller than that of visible light. Because of this, an EM can be used to study the atomic structure of materials. There are many different kinds of TEMs, of which only the scanning TEM (STEM), will be expanded upon here. Before discussing the STEM, however, the basics behind the TEM will now be presented. In a conventional TEM, a broad, parallel beam of electrons is transmitted through a sample. In order for a sufficient amount of electrons to be transmitted, the sample is required to be thin (a thickness of  $<100\text{ nm}$  is common). A TEM typically operates with electron energies of  $\approx 200\text{ keV}$  or  $300\text{ keV}$ , giving the electrons a velocity  $v > c/2$  which requires relativistic effects to be taken into account. Another factor that should be considered is the possibility of the electron beam damaging the material. This can happen as the chemical bonds in the material are broken (radiolysis), atoms are displaced or ejected from the crystal lattice (knock-on damage or sputtering, respectively) or as the material is changed due to heating [6].

### **2.2.1 Electron emission**

### **2.2.2 Electron-sample interaction**

When the electron beam hits the sample, several different signals are generated. This report will only discuss two of them: Characteristic X-rays (due to inelastically scattered electrons, and elastically scattered electrons. Characteristic X-rays are produced as the incoming electrons interact with inner-core electrons in the sample, and can be used to determine which elements the sample consists of. The theory behind characteristic X-rays, and why they are useful, will be expanded upon in section 2.3. Electrons being transmitted through the sample that are elastically scattered (that is, the energy of the incoming electrons is conserved) gives rise to a diffraction pattern, which can be used to determine the crystallographic properties of the sample. Electron diffraction will be properly introduced in Section 2.4 [6].

### **2.2.3 Scanning Transmission Electron Microscopy**

A scanning transmission electron microscope (STEM) uses an electron beam focused onto a small spot on the sample. The sample is then scanned in a raster pattern and the signal is recorded for each point. This technique can be used to investigate very small areas of the sample and accurately study transitions in atomic structure and/or composition.

## **2.3 X-ray spectroscopy**

The characteristic X-rays resulting from inelastic scattering of the electrons being transmitted through the sample can be used for both qualitative and quantitative analysis. Qualitative analysis can determine which elements are in the sample, while quantitative analysis can indicate the composition of the different elements. When X-ray spectroscopy is performed in a STEM, the electron probe is scanned over the material and focused on each pixel for a certain amount of time. During this time period, the X-rays being emitted from the sample are detected and the signal for the pixel is saved before the probe moves to the next pixel.

### 2.3.1 Energy-Dispersive X-Ray Spectroscopy (EDS)

#### X-ray emission

As previously mentioned, characteristic X-rays are produced due to inelastic scattering of the incoming electrons on the sample. If an electron reaches the inner-shell electrons of an atom in the sample, and a sufficient amount of energy is transferred to the inner-shell electron, the electron will be ejected from the nucleus. That is, it reaches an energy above the Fermi level and is no longer bound to the nucleus [CHECK THIS]. The atom is now in an excited state, and will seek to return towards its ground state. This leads to an electron in an outer shell taking the place of the ejected electron in the inner shell, and in the process emitting an X-ray or an Auger electron (Auger electrons will not be discussed further). If an X-ray is emitted, its energy will be characteristic of the specific element, as different elements have different critical ionization energies. The critical ionization energy is the energy required for an inner-shell electron to be ejected from the nucleus.

There will not necessarily only be emitted one characteristic X-ray for each hole created in the inner shell of an atom. This is because the outer-shell electron filling the hole will create a new hole in its shell, which must be filled by an electron in a shell even further out, and maybe emitting another characteristic X-ray. This process continues until there is a hole in the outermost shell of the atom that can be filled by an electron in the conduction or valence band of the material. The energy of the characteristic X-rays will also depend on which transition it is emitted because of. In addition, due to quantum effects the electron shells might be split into several sub-shells, further increasing the number of different energies the emitted X-rays can have.

The probability for a specific transition to occur must also be taken into account. If a transition between two specific shells has a relatively high probability compared to other transitions in the element, more characteristic X-rays with the corresponding energy will be emitted over a certain time period. This will lead to higher peaks in the EDS spectrum, which will be discussed shortly.

## X-ray detection

When doing EDS in a TEM, an X-ray detector is positioned above the sample to detect the X-rays emitted from it. The detector then measures the energy of each incoming X-ray, with a given energy resolution. If the measurement is done using STEM, the electron probe is scanned over the sample and kept at each pixel for a certain amount of time during which emitted X-rays are detected. When the scanning is complete, this results in a three dimensional EDS spectrum.

## EDS spectrum

In an EDS spectrum, the intensity of the X-rays is plotted against the energy of the X-rays. The intensity at a certain energy refers to the number of counts, that is, how many X-rays with that energy that were detected by the detector. An example of an EDS spectrum is shown in Figure 2.2. By consulting a table of known X-ray energies for the emission lines from different elements, for example [7], one can determine which elements are present in the sample. However, knowing which elements are present is not enough to determine the structure of the material. A next step can be to perform quantitative analysis on the same spectrum.

### 2.3.2 Quantitative X-ray Analysis

Quantitative analysis of an EDS spectrum gives information about the composition of the different elements in the material. A quantitative analysis might result in learning that an unknown material is a compound of a few different elements. In order to determine which compound this is, quantitative analysis is necessary.

There are primarily two methods for quantitative X-ray analysis: The Cliff-Lorimer ratio technique and the  $\zeta$ -factor method. The basis for both is assuming that the concentration of an element in a material is proportional to the intensity of characteristic X-rays being emitted from it,  $C \propto I$ .

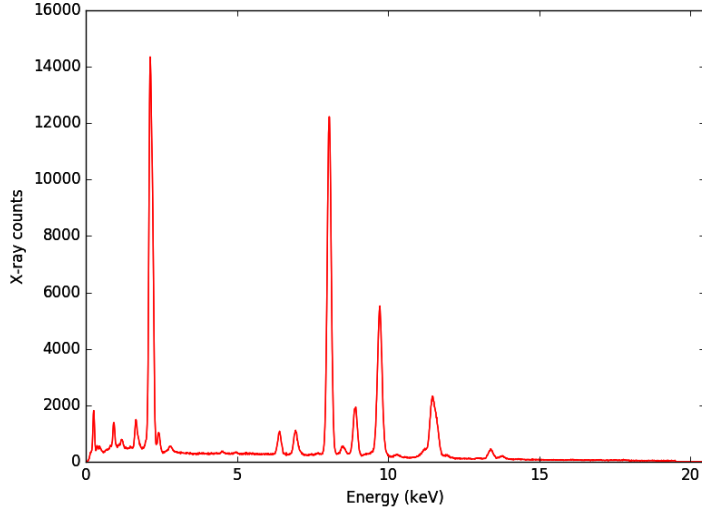


Figure 2.2: Example of EDS spectrum

### The Cliff-Lorimer ratio technique

The Cliff-Lorimer ratio technique, first introduced in 1972 [8], assumes that the weight percent ratio of two elements is proportional to their intensity ratio,

$$\frac{C_A}{C_B} = k_{AB} \frac{I_A}{I_B}, \quad (2.1)$$

where  $C_A$  is the weight percent,  $I$  is the intensity of the characteristic X-rays and the proportionality factor  $k_{AB}$  is called the Cliff-Lorimer factor, or the  $k$ -factor. The  $k$ -factor depends not only on the properties of the elements  $A$  and  $B$ , but also on the instruments used, the conditions under which the experiment was done, and how the intensities are extracted from the spectrum. This technique has several drawbacks: Firstly, determining the  $k$ -factor experimentally is very time-consuming, but a theoretical calculation can have a severe error [6]. And secondly, the multi-element thin standards necessary for experimental determination are difficult to prepare.

## The $\zeta$ -factor method

The  $\zeta$ -factor method was introduced by M. Watanabe and D. B. Williams in 1996, and overcomes several of the problems with the Cliff-Lorimer technique. If the material is a thin-film, its mass-thickness can be assumed to be proportional to the intensity of the characteristic X-rays  $I$  and the composition  $C$ ,

$$\rho t = \zeta \frac{I}{CD_e}, \quad (2.2)$$

where  $\rho$  is the density of the material,  $t$  is its thickness and  $D_e$  is the total amount of electrons that hit the material during the measurement.

Using the thin-film approximation to find a theoretical expression for the intensity  $I$ , the proportionality factor  $\zeta$  can be found to be

$$\zeta = \frac{M}{N_v Q \omega a [\Omega/(4\pi)] \epsilon}. \quad (2.3)$$

Here,  $M$  is the atomic weight,  $N_v$  is Avogadro's number,  $Q$  is the ionization cross section,  $\omega$  is the fluorescence yield,  $a$  is the relative transition probability,  $\Omega/(4\pi)$  is the detector collection-angle and  $\epsilon$  is the detector efficiency [9]. If the composition and thickness of a material is known, equation (??) can be used to calculate the  $\zeta$ -factor for the material.

Another advantage of the  $\zeta$ -factor method is the inclusion of absorption correction. The absorption correction-term for a specific X-ray line is given as

$$A = \frac{(\mu/\rho)_{sp} \rho t \text{cosec}(\alpha)}{1 - \exp[-(\mu/\rho)_{sp} \rho t \text{cosec}(\alpha)]}, \quad (2.4)$$

where  $(\mu/\rho)$  is the mass absorption coefficient for the specific X-ray line, and  $\alpha$  is the X-ray take-off angle. Absorption correction is implemented by multiplying this term to the intensity  $I$  in Eq. (2.2), giving

$$\rho t = \zeta \frac{I}{CD_e} A \quad (2.5)$$

In a multi-element system, assuming the compositions obey  $\sum_j C_j = 1$ , Eq. (2.2) gives the mass-thickness and composition of each element as

$$\rho t = \sum_j \frac{\zeta_j I_j A_j}{D_e}, \quad C_i = \frac{\zeta_i I_i A_i}{\sum_j \zeta_j I_j A_j} \quad (2.6)$$

These equations can be solved through an iterative process: First, the mass-thickness and compositions are determined without absorption correction. Then the correction terms are calculated, and the mass-thickness and compositions are calculated with absorption correction. These last two steps are repeated until convergence is reached [9].

As both the  $\zeta$ -factor and the  $k$ -factor in Eq. (2.2) and ?? are proportional to the X-ray intensity and composition, the ratios for two elements should be roughly equal,

$$\frac{\zeta_A}{\zeta_B} \approx k_{AB} = \frac{k_{AX}}{k_{BX}}, \quad (2.7)$$

where  $X$  denotes the element which the  $k$ -values have been measured with respect to.

### 2.3.3 Thickness estimation

The thickness of a sample can be estimated by using electron energy-loss spectroscopy (EELS), in which the energy which electrons lose due to inelastic scattering is measured. From Poisson statistics, the mean number of scattering events for each electron can be calculated from the EELS spectrum as

$$t/\lambda = \ln(I_t/I_0), \quad (2.8)$$

where  $I_0$  and  $I_t$  are the areas under the zero-loss peak and under the whole spectrum, respectively. If the mean free path  $\lambda$  is known, the thickness  $t$  can be estimated [10, 11].

## 2.4 Electron diffraction

When electron diffraction is performed in a TEM, a beam of electrons is transmitted through the specimen. As the electrons pass through, some are scattered due to the atomic potentials in the specimen. By detecting the positions of the electrons after they have been transmitted through the specimen, a diffraction pattern is obtained. Analyzing this diffraction pattern can determine the characteristics of the specimen, for example whether it is crystalline or amorphous, if there are several phases present, and if crystalline, what its crystallographic characteristics are. This information can not be obtained through EDX.

Electron diffraction in a STEM, or scanning electron diffraction (SED) works similarly to EDX in STEM: A parallel electron probe is scanned over the specimen in a raster pattern, and the resulting 2-dimensional diffraction pattern is recorded for each pixel. The result is a 4-dimensional dataset: Two axes in real space and two in reciprocal space.

### 2.4.1 Diffraction theory

When discussing the diffraction of electrons, it is convenient to regard the electrons as waves. When a parallel electron wave with a wave vector  $\vec{k}_i$  reaches the specimen, the electrons will scatter to different angles  $\theta$ . Assuming the scattering is purely elastic, i.e. the energy of the electrons is conserved, the wave vectors of the scattered electrons will be equal in magnitude to the wave vector of the incoming electrons,  $|\vec{k}_s| = |\vec{k}_i| = {}^1\lambda$ .

+++ figure here

?? shows two electrons being scattered from atoms at two different atomic planes separated by a distance  $d$ . After being scattered, the distances the electrons have traveled differs by  $2d \sin \theta$ , where  $\theta$  is the scattering angle. If this path difference is equal to an integer number of wavelengths, the electrons' phases will be equal. The angles  $\theta$  where this occurs are called the Bragg angles, and this condition is called Bragg's law, given by

$$2d \sin \theta_B = N\lambda, \quad (2.9)$$

where  $N$  is an integer.

The equivalence of Bragg's law in reciprocal space is the Laue condition. In order to discuss this, a few definitions must be made. First of all, the scattering vector  $\vec{Q} = \vec{k}_s - \vec{k}_i$  describes the change in the wave vector due to diffraction. The resulting phase difference between the two scattered electrons can thus be written as  $\Delta\phi = \vec{R} \cdot \vec{Q}$ , where  $\vec{R}$  gives the position of the second atom relative to the first. To generalize this, note that any three-dimensional lattice can be described by a set of vectors

$$\vec{R}_n = n_1 \vec{a}_1 + n_2 \vec{a}_2 + n_3 \vec{a}_3, \quad (2.10)$$

where the vectors  $\vec{a}_i$  are called the lattice vectors, and  $n_i$  are integers. If the phase difference is to be equal to zero, so that Bragg's law (Eq. (2.9)) is fulfilled, we get the condition

$$\vec{R}_n \cdot \vec{Q} = 2\pi N, \quad (2.11)$$

where  $N$  is an integer. To solve this equation, let us first define the reciprocal lattice. Similarly to the definition of the real-space lattice in Eq. (2.10), the reciprocal lattice can be defined as

$$\vec{G}_{hkl} = h\vec{a}^*_1 + k\vec{a}^*_2 + l\vec{a}^*_3, \quad (2.12)$$

where  $h$ ,  $k$  and  $l$  are integers, and the vectors  $\vec{a}^*_i$  satisfy the condition

$$\vec{a}^*_i \cdot \vec{a}_j = \delta_{ij},$$

where  $\delta$  is the Kronecker delta. It is now seen that the reciprocal lattice vectors  $\vec{G}$  satisfy Eq. (2.11), as the scalar product  $\vec{G} \cdot \vec{R}_n$  is an integer. The Laue condition can now be written as

$$\vec{Q} = \vec{G} \quad (2.13)$$

In other words, there will be constructive interference only when the scattering vector  $\vec{Q}$  equals a reciprocal lattice vector  $\vec{G}_{hkl}$ .

The Laue condition can be visualized through the Ewald sphere construction. Section 2.4.1 shows the reciprocal lattice, the wave vectors of the incoming

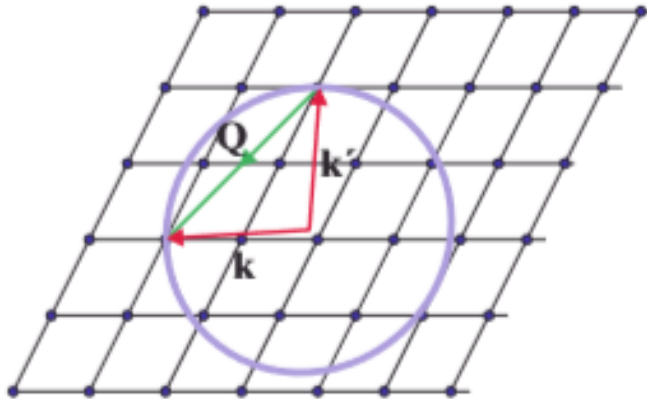


Figure 2.3: Ewald sphere. From Modern x-ray physics.

and the scattered waves, and a circle with radius  $|\vec{k}_i| = \lambda^{-1}$ . The incoming wave vector  $\vec{k}_i$  terminates on a reciprocal lattice point, which is where the diffracted wave vector  $\vec{k}_s$  originates.  $\vec{k}_s$  can terminate anywhere on the Ewald sphere, but the Laue condition will be satisfied only if it terminates on a lattice point.

#### 2.4.2 Electron diffraction in STEM

#### 2.4.3 Scanning Precession Electron Diffraction (SPED)

Scanning precession electron diffraction (SPED) is a modification of SED. Fig. 2.4 shows the schematic of SPED. The electron beam is now tilted a fixed angle  $\phi$  and precessed around the vertical axis. The beam will hit the sample at the same spot during the precession; only the direction of the incoming beam will be changed. The diffracted beam is also precessed so that the locations of the diffraction spots remain fixed during the precession.

There are several reasons why adding precession to electron diffraction gives better results. The perhaps most important is that the Ewald sphere is precessed in reciprocal space. This causes the Laue condition to be fulfilled for

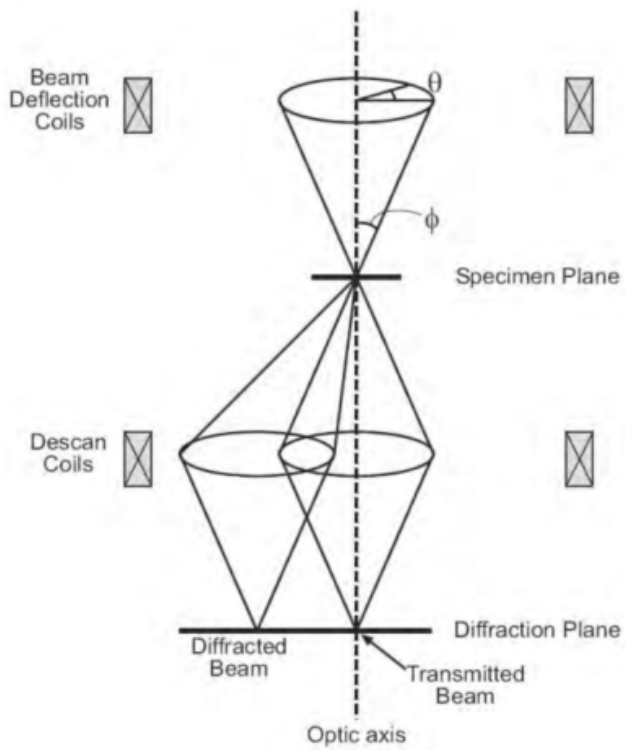


Figure 2.4: Figure from [12]

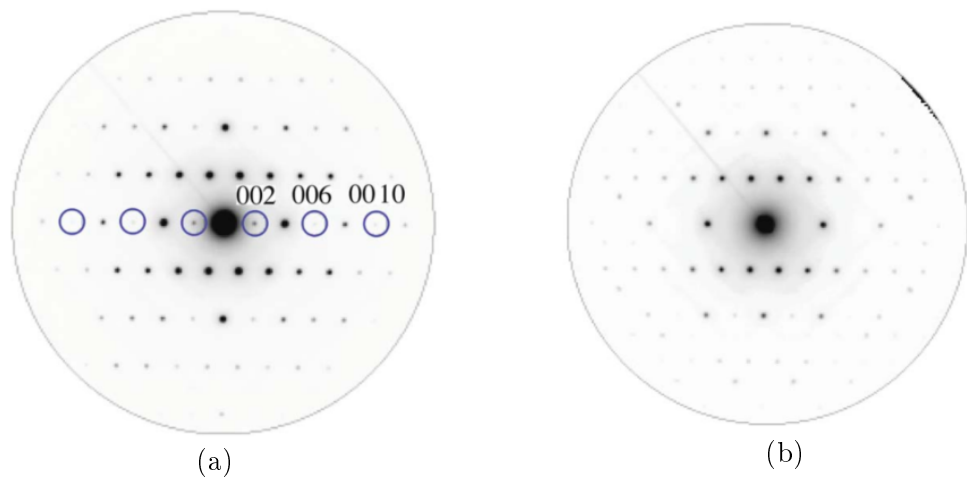


Figure 2.5: From [6]

a higher number of reciprocal lattice points, resulting in more visible spots in the diffraction pattern. Another major improvement is the reduction of dynamical effects, in particular double diffraction, in the diffraction pattern. Double diffraction occurs when an electron is scattered twice, and can result in diffraction spots appearing even though they do not satisfy the Laue condition. As the beam is being precessed, dynamical effects are to a large extent averaged out [6, 12]. Fig. 2.5 shows an example of how using a larger precession angle causes a reduction of dynamical effects.

## 2.5 Data analysis

### 2.5.1 Template matching

Template matching is used for finding the location in a reference image where a template image fits best. The function *MatchTemplate* in the python library OpenCV does this by sliding the template image over the reference image, and recording how well it fits at each point. This matching value is given as the normed square difference between the two images for each pixel in the reference image:

$$R(x, y) = \frac{\sum_{x',y'} (T(x', y') - I(x + x', y + y'))^2}{\sqrt{\sum_{x',y'} T(x', y')^2 \cdot \sum_{x',y'} I(x + x', y + y')^2}} \quad (2.14)$$

Here,  $(x, y)$  are the coordinates of the reference image,  $(x', y')$  the coordinates of the template,  $I(x, y)$  is the value of the pixel  $(x, y)$  in the reference image and  $T$  likewise in the template. The matching value  $R(x, y)$  can take any value between 0 and 1, where 0 means a perfect match and 1 a perfect mismatch.

### 2.5.2 Re-binning and rotating multidimensional data

Attempting to re-bin and rotate a multidimensional array can be problematic. A rotation that is not a multiple of 90 degrees will lead to jagged edges, and zero-values will have to be added to make it rectangular again. An even

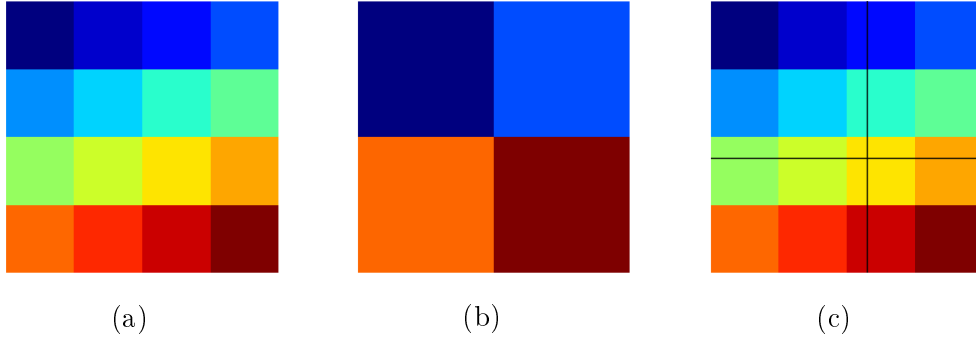


Figure 2.6: Rebin figures

bigger problem occurs when re-binning an array. If the new lengths along each axis are divisors of the original lengths, it is relatively easy. Fig. 2.6(a) shows a 4x4 array, where each value is visualized by a color. Rescaling this array by a factor of  $s = 2.0$  is simple as each value in the new array can be calculated as the mean of the corresponding 4 values (2x2 array) in the original array, resulting in the array in Fig. 2.6(b). This is called down-sampling, and causes information to be lost. Likewise, if re-binning the 4x4 by a factor of  $s = 0.5$ , each value in the original array now corresponds to four values (2x2) in the new 8x8 array. These four values can simply be given the same value as the one in the original array. This procedure is called up-sampling, and new information is added.

However, if the new lengths of the array are not divisible by the original lengths, the re-binning procedure is no longer as easy to conceptualize. Imagine that instead of a two-dimensional array we now have a 3-dimensional one, where two of the dimensions are in real space and the third in signal space. This is the format of EDX data taken in STEM mode. Rescaling the real-space axes of this array will necessarily also change the signal axis. One way to solve this problem is to linearly interpolate the signal. Let the array in Fig. 2.6(a) now denote the EDX dataset, with each color representing an EDX spectrum. If it is down-sampled by a scale factor of for example  $s = 2.3$ , it will become a 2x2 array as before. However, as shown in Fig. 2.6(c), it is no longer as trivial. The top left value will now consist of the sum of the 2x2=4 top left values in the original matrix, plus 30 percent of the 3rd row and column. In the same way, the bottom right value will be the sum of the 2x2=4 bottom right values in the original matrix, plus 70 percent of the

3rd row and column. The result will be similar to Fig. 2.6(b), except that the colors (or spectra) will be slightly different. This process is called linear re-binning.

# Chapter 3

## Experimental

### 3.1 Equipment

### 3.2 Material

### 3.3 Dataset matching

Several methods were attempted in order to match the SPED and EDX datasets. The goal was that the matching would be performed automatically with no human input. For this to happen, the code would have to scale, rotate and translate one of the the datasets so that it fit the other. The EDX dataset taken at the intersection of the nanowire and the other elements deposited on it shows a relatively clear separation, and is also the dataset covering the biggest area of the sample. As the SPED dataset was taken over a larger area than the EDX dataset, it was decided to attempt to locate the position of the EDX dataset in the SPED dataset.

The python library OpenCV contains an algorithm which uses template matching, described in Section 2.5.1, to find the best matching location of one image in another. The algorithm requires that the images are correctly scaled and rotated. To be used with this function, the two datasets first had to be processed to make them look more similar, and to enhance the border

of the nanowire. The signal space of each of the datasets was limited to only include signals corresponding to the nanowire. For the SPED dataset, this was done by inserting a virtual annulus that covered only one diffraction spot, which was unique for the nanowire. Similarly, in the EDX dataset, the spectrum was cropped to only include the characteristic  $K_{\alpha}$ -peaks of Ga and As. The signal dimension of the datasets were then averaged out, in order to convert them into 2-dimensional arrays, or equivalently, gray-scale images.

The images were now rotated and rescaled. The rotation angle was estimated by selecting two points along the same straight line in both images and finding the angle between them. In the HyperSpy metadata of each of the datasets, a scaling factor giving the size of each pixel was given. The SPED image was rotated through the estimated angle, and the EDX image was rescaled by the ratio between the scaling factors. In order to limit the error caused by manual estimation of the rotational angle, the template matching algorithm was run 30 times for angles in the range  $\pm 3\%$  of the manually estimated angle. In addition, because the contrast levels of the two images are not necessarily equal, the SPED image was multiplied by a gray-scale factor, ranging from 0.80 to 0.85 (this range was found experimentally to give the best results) through 30 steps.

For each of the  $30 \times 30$  iterations of the template matching algorithm, the matching value defined in Eq. (2.14) was calculated, and the angle and gray-scale factor giving the lowest matching value were obtained. As it was noticed that the scaling factors in the metadata appeared to be a bit off, making the EDX image slightly larger than it should be. A second iteration was therefore performed, in which the scale factor was multiplied by a factor ranging from 0.90 to 1.0. The algorithm was now iterated over 30 times for the scaling factor and 30 times for the contrast level. Lastly, all three parameters were iterated over simultaneously, 30 times for each.

After finding the position of the EDX image in the SPED image, the full datasets were processed to enable them to share the same navigation window (define this?). First, the SPED dataset was rotated using T. Aarholt's *rotate*-function [13], which is currently awaiting implementation into HyperSpy. Then, the EDX dataset was rescaled and re-binned using K. MacArthur's function *linear\_bin* [14], also awaiting implementation into HyperSpy. The functionality of this function is described in Section 2.5.2. Lastly, a portion of the SPED dataset, corresponding to the location of the EDX image found

earlier, was cut out. The two datasets now have the same number of pixels in real space, and each pixel corresponds to the same area of the sample. Using the *Mirror navigation*-function in HyperSpyUI [15], the two datasets can be made to share a navigation window.

It then remained to do this for the remaining datasets, all of which were smaller than the dataset used above. Instead of repeating the procedure, the HAADF image, which shows a large area of the sample, was used to find the positions of the remaining datasets with respect to the first. To do this, OpenCV template matching was used to locate the positions of all the datasets in the HAADF image. It was first attempted to use the EDX datasets, converted to images using the technique described earlier. This worked well for the datasets covering a relatively large region of the sample, but not for the smaller ones; therefore, survey images were used instead. These images are taken before the EDX recording, and shows a larger region of the sample (is this survey image also HAADF?).

The image matching now also required a change in the contrast level to give accurate results. The contrast levels were found experimentally for the unheated and the heat-treated datasets by iteration, and comparing the sum of the matching values for all the datasets. After image matching was complete, the matched region was cropped to the actual area of the EDX dataset. The coordinates of this area were found in the survey image's metadata in HyperSpy.

Lastly, the positions of the remaining datasets had to be found in the SPED dataset. The datasets were again scaled and re-binned to fit the SPED dataset, but now also the coordinates in the HAADF image had to be scaled to the SPED dataset, so that the correct area could be cropped out. This step has not been completed.

## 3.4 Quantitative analysis

]

The first step in the quantitative analysis was to determine the  $\zeta$ -factors of the elements in the sample. As this method had not yet been implemented into HyperSpy [5], the necessary code was acquired from the Master's the-

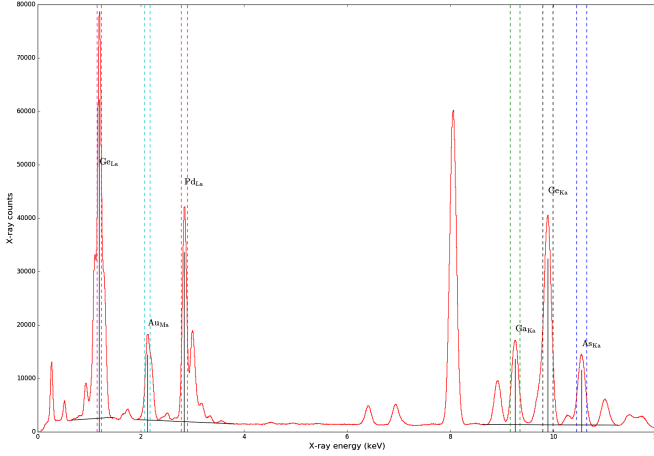


Figure 3.1

Table 3.1: All emission lines (from data booklet) in keV

Z	Element	$K_{\alpha 1}$	$L_{\alpha 1}$	$M_{\alpha 1}$
31	Ga	9.252	1.098	-
32	Ge	9.886	1.188	-
33	As	10.544	1.282	-
46	Pd	-	2.839	-
79	Au	-	9.713	2.123

sis of A. Garmannslund [16]. The thickness of the material was estimated using a thickness map (see Section 2.3.3). Background subtraction was performed by selecting an area of the background signal at both sides of each characteristic line, and drawing a line between the centers of these two areas. The intensities of the lines were then calculated by integrating over the peaks within an integration window of 1.2 FWHM. Fig. 3.1 shows the characteristic X-ray peaks that have been used, the background that has been subtracted, and the integration windows.

The thickness of the sample was estimated using the log-ratio method, given in Eq. (2.8). From an EELS map of the unheated sample, the average number of scattering events was found for the middle part of the nanowire. For the mean free path for GaAs,  $\lambda = 104$  was used [16].

The quantification of the samples was performed using three different methods: The Cliff-Lorimer ratio technique, for which the necessary  $k$ -factors were obtained from the TEM software; the  $\zeta$ -factor method; and the  $\zeta$ -factor method with background subtraction. HyperSpy was used for the first two of these methods, but absorption correction is at the time not been included in the software. The necessary code for this was also acquired from Garmanzlund's thesis. All three techniques were used in order to enable the results to be compared against each other. In an attempt to verify the techniques, they were first used on the untreated sample whose composition is assumed to be known. They were then used on the heated sample in order to determine the composition at locations of interest.

The choice of which characteristic peaks were used for the quantifications of different areas in the sample needs to be addressed. First of all, as seen in ??, there are large overlaps between several of the characteristic peaks of the elements in the sample. Because of the overlap between the  $Ge_{K\alpha}$  and the  $Au_{M\alpha}$ , these two peaks could not be used simultaneously during the quantification process. Further, however, there is also a large overlap between the  $L_\alpha$ -peaks of Ga, Ge and As, making it difficult to accurately measure the compositions of these four elements simultaneously, because, as Table 3.1 shows, there are no more peaks within the energy range used in the TEM that give many enough counts to be used for quantification.

For this reason, for the regions in the heated sample, two separate quantification processes were performed: First with the  $K_\alpha$ -peaks of Ga, Ge and As, and the  $L_\alpha$ -peak for Pd, and second with the  $L_\alpha$ -peaks of Ga, Ge, As and Pd, and the  $M_\alpha$  for Au. This second quantification must now be understood to not give accurate results if all three elements Ga, Ge and As are present in the analyzed region.

# Chapter 4

## Results

The results will be introduced in the same order as the experiments were conducted. First, the results of matching of one of the EDX datasets with the SPED dataset will be presented. This is followed the position matching of the various EDX datasets with the overview images. Lastly, the calculated  $\zeta$ -factors and the quantification of the samples using the  $\zeta$ -factor method and the Cliff-Lorimer technique are displayed.

### 4.1 Dataset matching

Fig. 4.1 shows the results of matching the largest EDX dataset with the SPED dataset. Fig. 4.1(a) shows the first result, with the SPED dataset rotated by the manually estimated angle, and the EDX dataset scaled using the scale factor obtained from the metadata. In Fig. 4.1(b), the angle has been iteratively optimized, and therefore increased by 0.4% (0.4 deg). Fig. 4.1(c) shows the third result, where only the scale factor has been optimized. The lowest matching value was found if the scale factor was reduced by 6.5%. The final attempt, in which both the rotation angle and the scale factor were iterated, resulted in the angle being increased by 2.8% (2.6 deg) which was clearly too much. Should processed images be shown as well? In Figs. 4.1(a) and 4.1(b) the results are very similar, and it appears from the nanowire that the EDX image is larger than the SPED image. In Fig. 4.1(c), on the other hand, the EDX image appears slightly smaller than the SPED image.

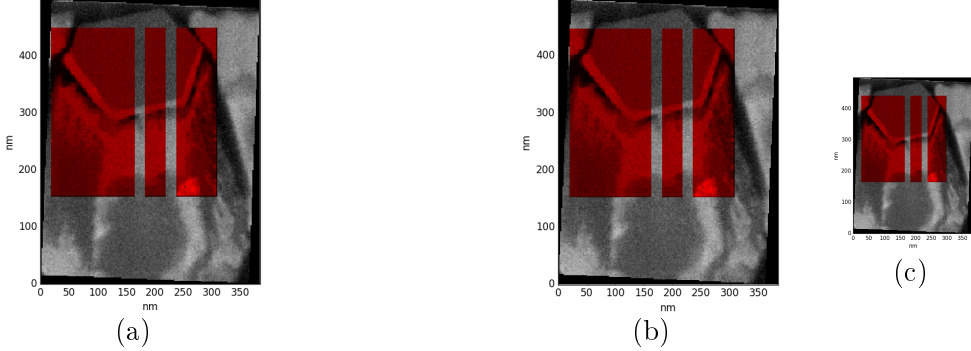


Figure 4.1: Caption

The results from locating the EDX datasets in the HAADF overview images are displayed in Fig. 4.2(a) and ?? for the non-treated and the heat-treated samples, respectively. In the non-treated sample, the two datasets B and D were not correctly located in the overview image. The calculated location of dataset B was completely off, while the position of D was just slightly offset. The actual positions of these datasets were estimated by eye and marked in Fig. 4.2(a) as blue dotted rectangles. The rest of the datasets were located correctly, and their positions are shown as red rectangles. For the heat-treated sample, all the datasets that were included in the overview image were correctly located. However, the areas covered by two the datasets A and B were found to not be included in the overview image.

The accuracy of the matching for the different datasets are shown in Fig. 4.2(b) for the non-heated sample, and in Fig. 4.3(b) for the heated values. The horizontal axis shows the different datasets while the vertical axis is the matching value in percent, where 100 % is defined to be the matching value of the dataset covering the biggest area in each respective sample. The matching of this dataset is assumed to be the most trustworthy due to there being fewer potential locations that resemble the actual location, as there are several distinct features. For the smaller datasets, or more accurately, the datasets with smaller survey images, there might be several different locations in the overview image that all give a fairly good match.

In both figures, the red star is the value of the dataset used as reference, the red circles are the correctly matched datasets while the blue squares are the datasets that resulted in a wrong location. The non-heated sample

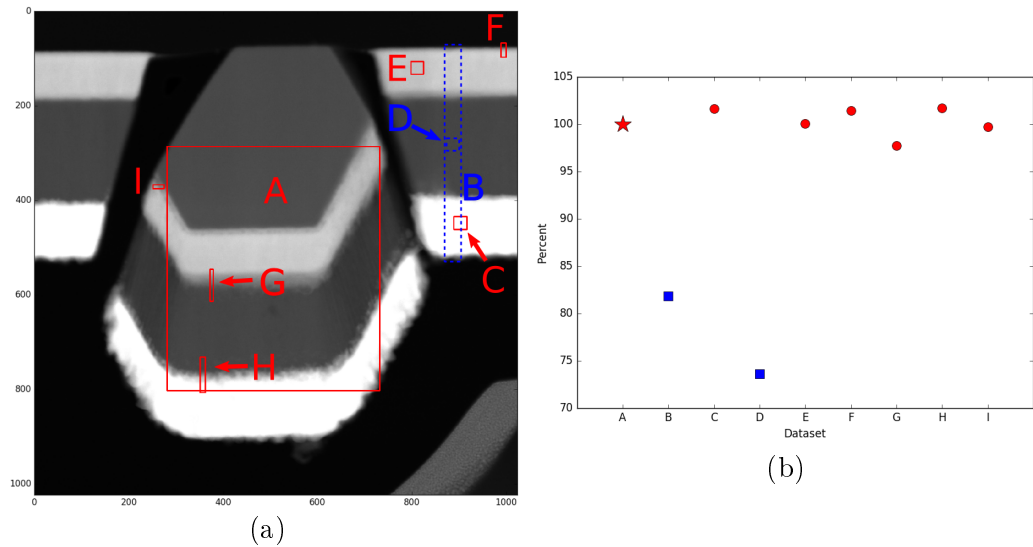


Figure 4.2: Nonheated edx in sped

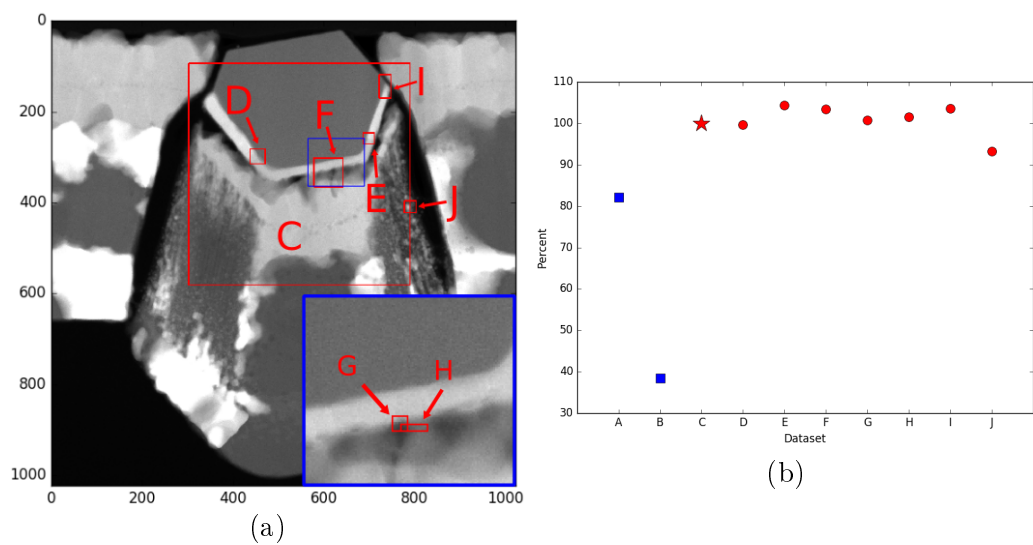


Figure 4.3: Heated edx in sped

(Fig. 4.2(b)) shows high values for all the correctly located datasets, and significantly lower values for the wrongly located ones. In addition, it must be noted that the exact location of dataset F was impossible to verify visually due to the survey image not being large enough to distinguish specific features. In the heated sample (Fig. 4.3(b)), all the red correctly located datasets have high values while the datasets that were not present in the reference image have distinguishably lower values.

## 4.2 Determination of $\zeta$ -values

The calculated  $\zeta$ -values for all the characteristic X-ray lines used to quantify the data are presented in Table 4.1, along with which dataset was used to calculate them. The calculated  $\zeta$ -values were compared to the corresponding  $k$ -values using Eq. (2.7), with  $\text{Ga}_{K\alpha}$  as reference element. Fig. 4.4 shows the results, with the mean value and spread of the  $\zeta$ -factors indicated. The average  $\zeta$ -values have been used for all further calculations.

Table 4.1: zeta values

Element	Dataset	$K_\alpha$	$L_\alpha$	$M_\alpha$
Ga	C*	486	512	-
Ga	A	608	826	-
As	C*	576	600	-
As	A	706	955	-
Ge	B	729	898	-
Ge	D	740	901	-
Ge	A	745	933	-
Pd	E	-	1249	-
Pd	A	-	1284	-
Pd	B	-	1316	-
Au	B	-	3422	2396
Au	C	-	3426	2387

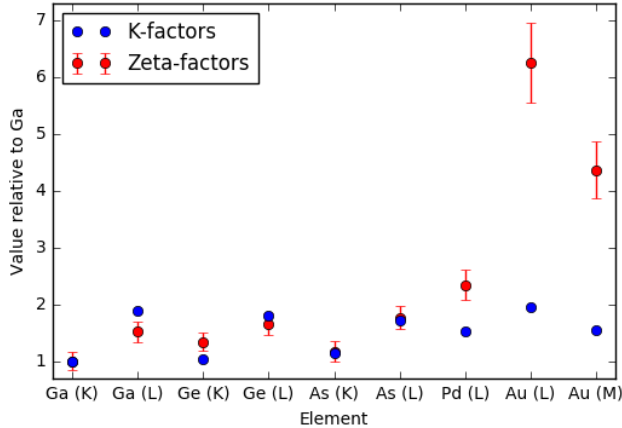


Figure 4.4: zeta - k - comparison

### 4.3 Quantification

Figs. 4.5 and 4.6 shows the compositions of two areas (Figs. 4.5(a) and 4.6(a) shows the locations of these areas) in the untreated sample, as calculated using the Cliff-Lorimer ratio method (CL method) and the  $\zeta$ -factor method with and without absorption correction. All the spectra have been averaged in the horizontal direction. The results are as expected. Figs. 4.5(b) and 4.5(c) shows that the nanowire consists of Ga and As in a 50:50 ratio, and Figs. 4.5(d) and 4.5(e) shows that the next two layers are approximately 100% Pd and 100% Ge, respectively. In the second area, Figs. 4.6(b) to 4.6(d) shows that the composition of elements are approximately 100% Au in the top region, 100% Pd in the middle and 100% Ge in the lower region.

All three techniques give fairly similar answers for Ga and As, while the differences between the CL- and  $\zeta$ -factor methods are significantly higher for Pd, Ge and Au. The inclusion of absorption correction does not give very different results for any of the elements, except for the Ge-region in the second area where the absorption correction appears to significantly amplify two erroneous peaks. There is a clear transitioning length between each of the elements layers where the spectra shows characteristic peaks belonging to both elements. This length is shortest for the transition between GaAs and Pd, and longest between Pd and Ge.

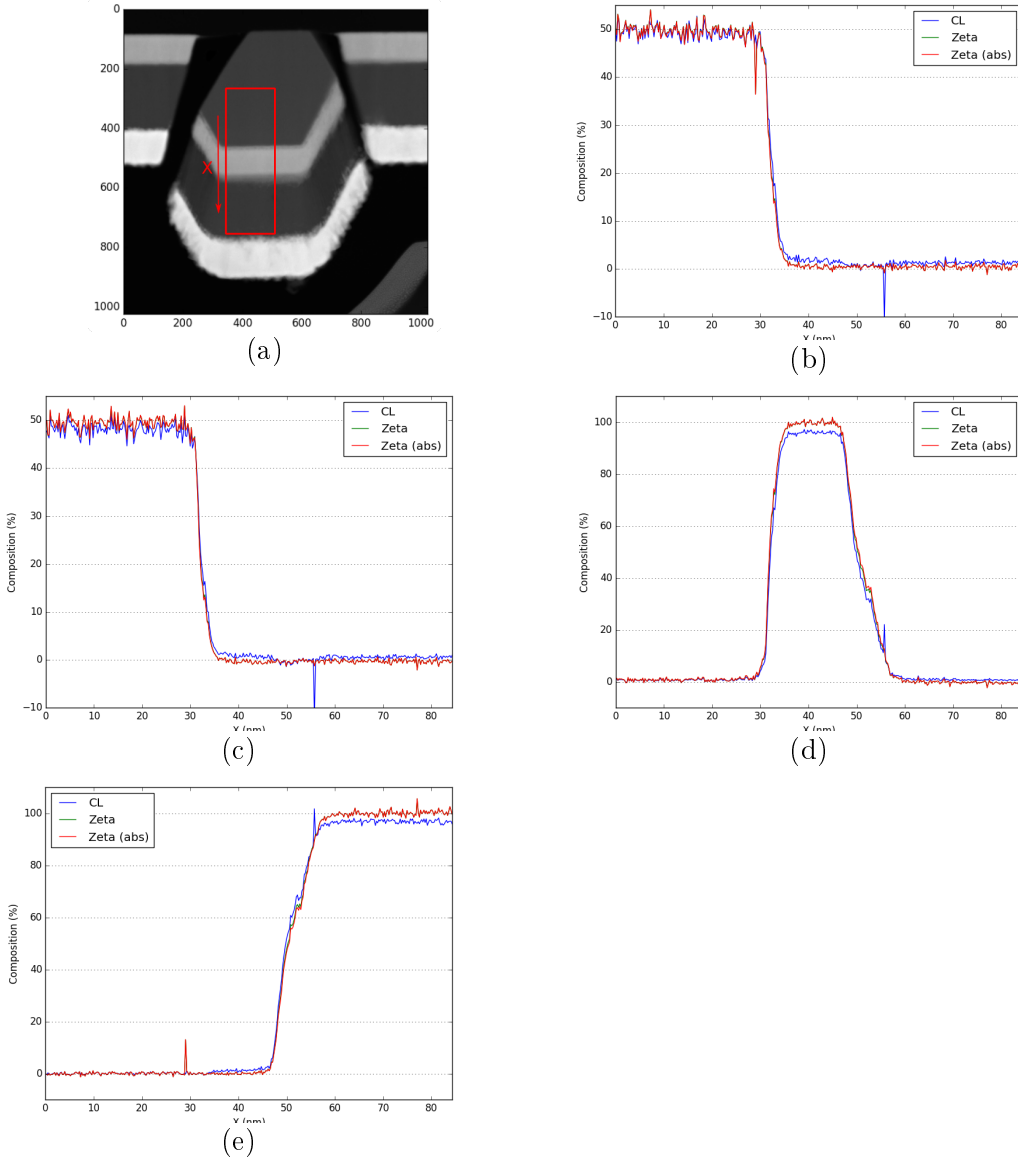


Figure 4.5: plots of....

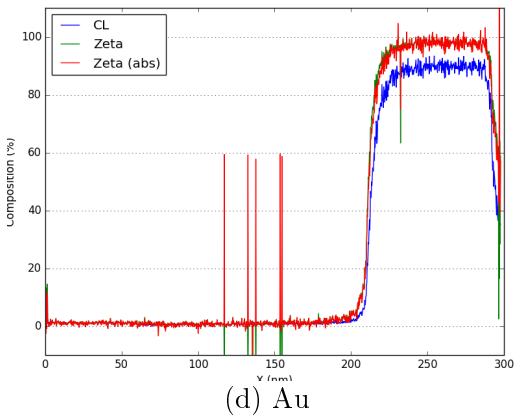
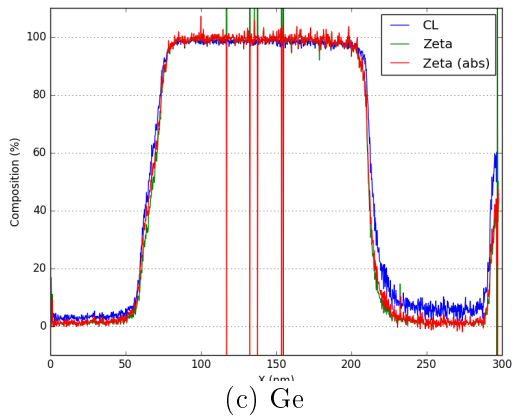
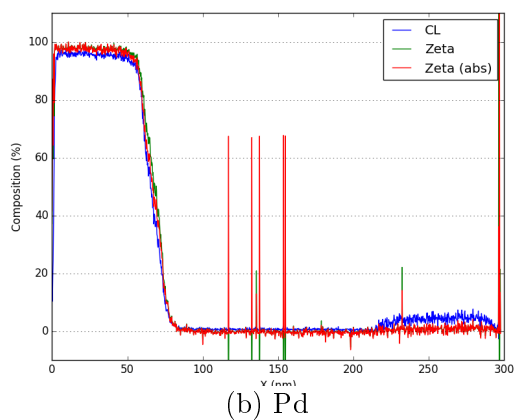
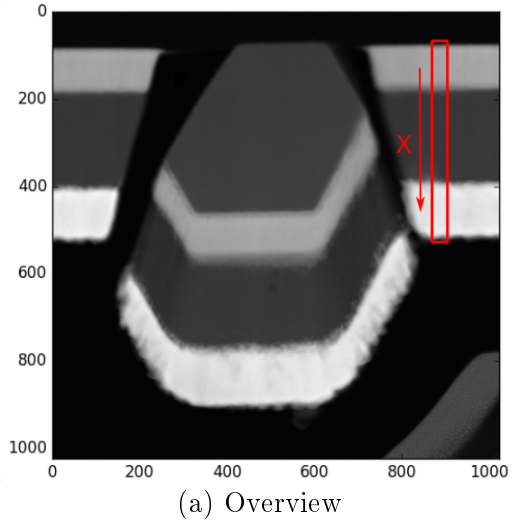


Figure 4.6: plots of....

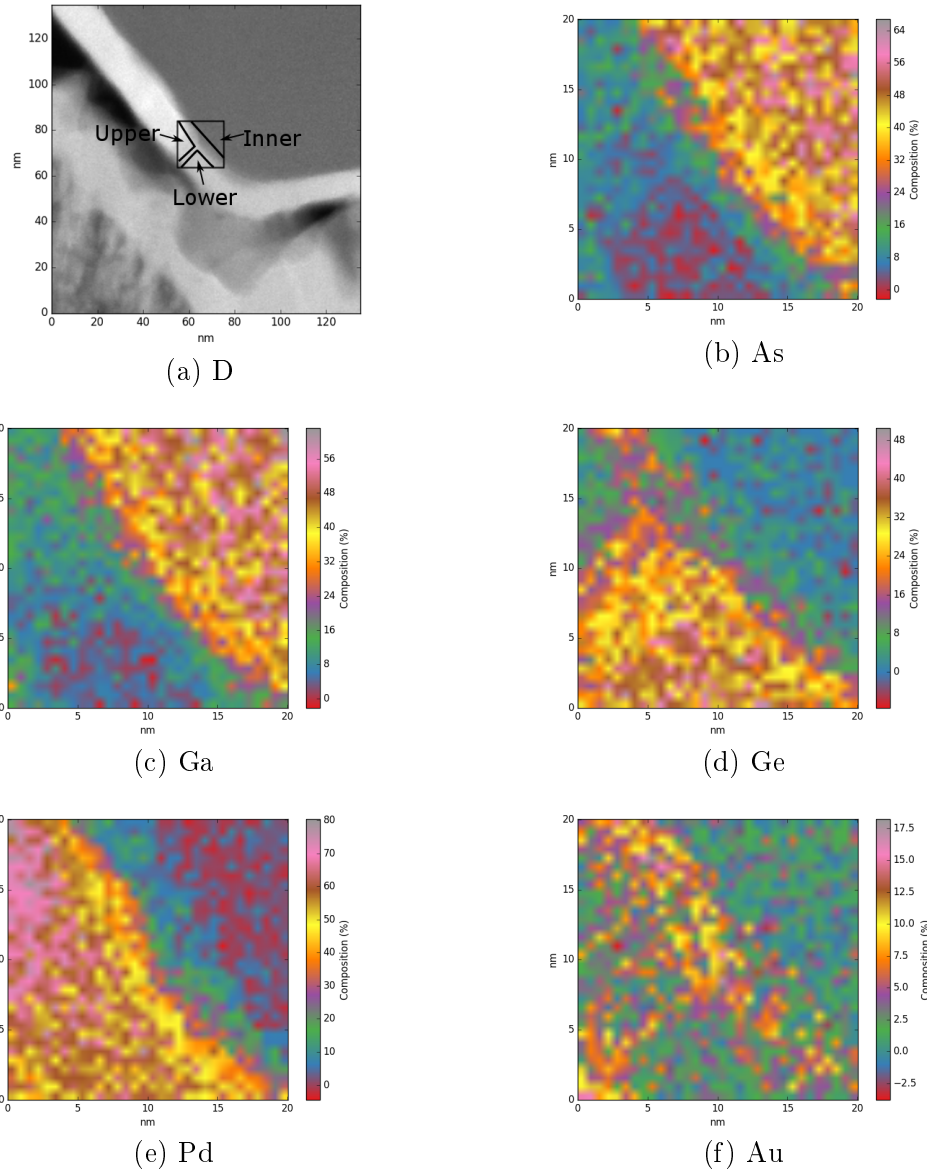


Figure 4.7: plots of....

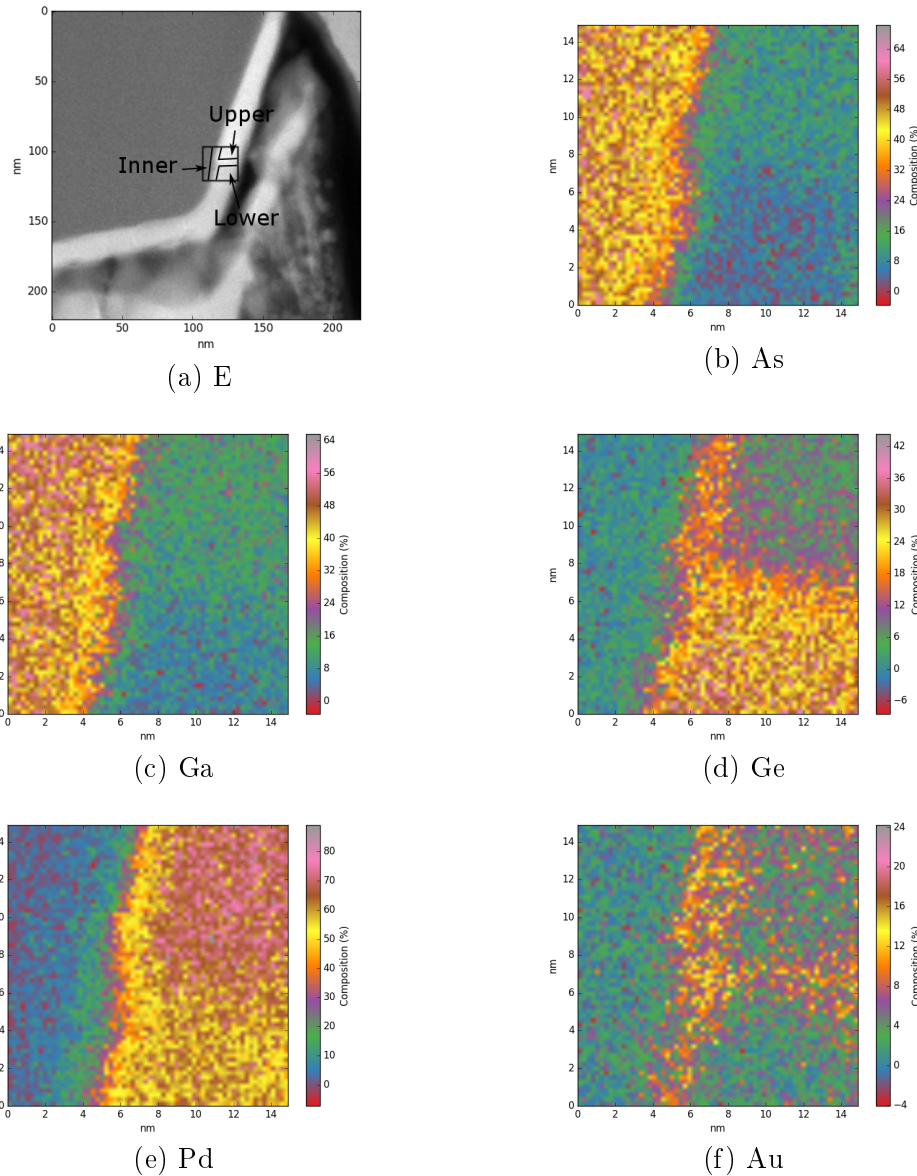


Figure 4.8: plots of....

Table 4.2: For area D (zeta). Parentheses: abs correction

Area	Ga	As	Ge	Pd	Au
Inner	40-60	40-60	0-7	0-7	0-2
Lower	3-10	3-10	30-40	50-60	0-4
Upper	5-15	5-15	5-18	65-80	2-6

The resulting compositions from areas D and E in the heat-treated sample, using the  $\zeta$ -factor method without absorption correction, are shown in Figs. 4.7 and 4.8. The areas D and E are located, as seen in Figs. 4.7(a) and 4.8(a), in the melted region on the left and right side of the nanowire, respectively. As previously explained, it was not possible to get accurate compositions of all elements simultaneously. Therefore, the quantification was done in two stages. The first time with Ga, As, Ge and Pd, using the  $K_\alpha$ -peaks for Ga, As and Ge, and the  $L_\alpha$ -peak for Pd. As seen in Fig. 3.1, this gives clear and distinct peaks for all the element, and is therefore expected to give accurate results. The second time was performed using all the elements, but now with the  $L_\alpha$ -lines for Ga, As, Ge and Pd, and the  $M_\alpha$ -line for Au. This causes a high degree of overlap between the Ga-, As- and Ge-lines, and will therefore overestimate the composition of these elements compared to Pd and Au. These results are therefore not included except for Au, in order to give an indication of the measured composition. Figs. 4.7(b) to 4.7(e) and 4.8(b) to 4.8(e) are calculated using the first method, while Figs. 4.7(f) and 4.8(f) are from the second method.

Tables 4.2 and 4.3 provides a summary of the compositions of areas D and E, respectively, in which the areas have been roughly divided into three regions, as shown in Figs. 4.7(a) and 4.8(a). Maps showing the compositions calculated using the CL-method and the  $\zeta$ -factor with absorption correction are given in ???. The results from the  $\zeta$ -factor with absorption correction were mostly very similar to the ones without absorption correction (with a maximum deviation of about 1 pp.), while the CL-method caused offsets by up to 12pp.

Fig. 4.9(a) shows three areas whose average compositions were calculated using all three techniques, and again two separate calculations were performed. Fig. 4.9(b) shows the results when using the  $K_\alpha$  peaks of Ga, As and Ge, and the  $L_\alpha$ -peak of Pd, while Fig. 4.9(c) was calculated using the  $L_\alpha$  peaks of Ge

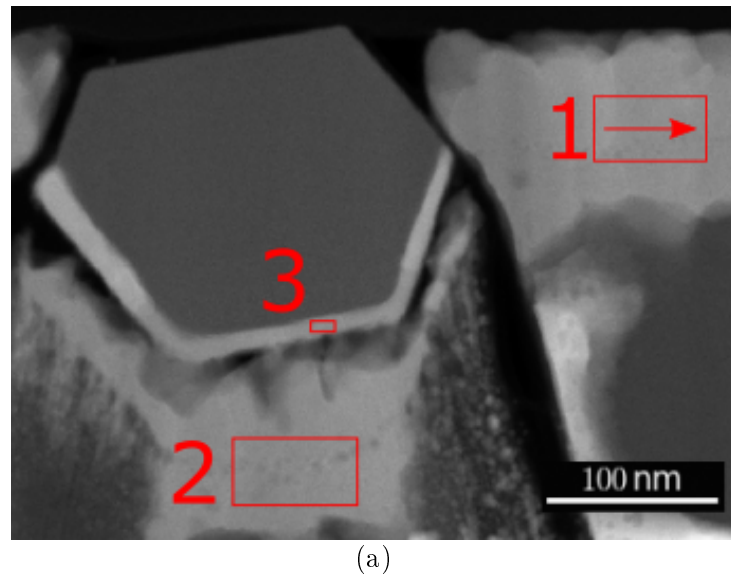
Table 4.3: For area E (zeta). Parentheses: abs correction

Area	Ga	As	Ge	Pd	Au
Inner	40-60	40-60	0-5	0-10	0-2
Lower	0-10	0-10	25-35	50-60	0-6
Upper	5-15	5-15	5-12	65-80	2-10

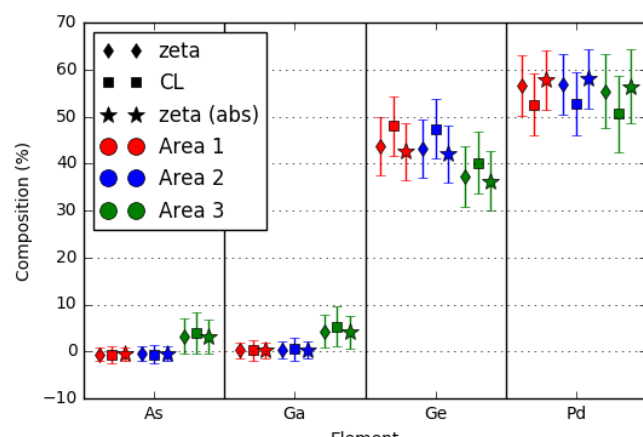
and Pd, and the  $M_\alpha$ -peak of Au. The latter calculation was performed using the  $L_\alpha$ -lines of Ga and As as well, but this calculation gave compositions of 10-15% As and 5-10% Ga in all areas, which is clearly not consistent with Fig. 4.9(b), which is also assumed to give more accurate results for Ga and As due to less peak overlap. The figures also shows the standard deviations of the calculated compositions.

It is clear from Fig. 4.9(b) that areas 1 and 2 contain no Ga or As, while area 3 contains about 5% of each, and the three different methods give very similar results for these elements. For Ge and Pd, the  $\zeta$ -methods with and without absorption correction both give a composition of about 40-45 % Ge and 55-60 % Pd for areas 1 and 2, and 35-40% Ge and 55-60 % Pd for area 3. The CL-method results in approximately 5 pp more Ge and 5 pp less Pd in all areas, compared to the  $\zeta$ -methods. The differences between the  $\zeta$ -method with and without absorption correction are consistently only about 1-2 pp.

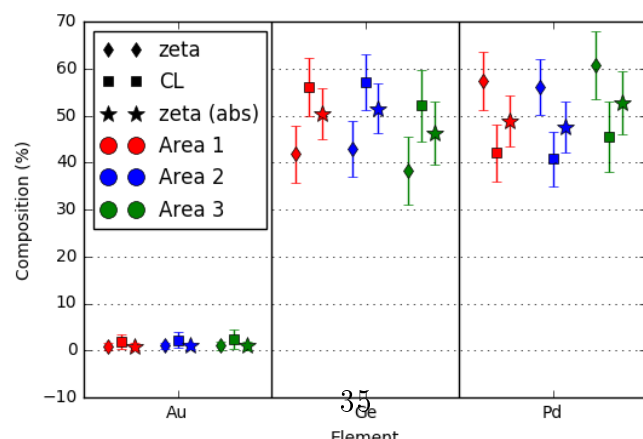
Fig. 4.9(c) gives slightly different results. It must here be noted that these results will be very inaccurate for area 3, which from Fig. 4.9(b) contains Ga and As, which is not included in this quantification process. Both  $\zeta$ -methods now report little or no presence of Au in all areas, while the CL method gives a few percent. In areas 1 and 2, both the CL-method and the  $\zeta$ -method with absorption correction reports that the ratios of Ge to Pd have been offset by up to more than 10 pp, compared to Fig. 4.9(b). On the other hand, the  $\zeta$ -method without absorption gives approximately the same values for Ge and Pd; the Ge:Pd ratio has been skewed by a few percent at most.



(a)



(b)



(c)

Figure 4.9: Caption

# Chapter 5

## Discussion

### 5.1 Dataset matching

- How good is the matching in the three different cases. Rotation and scale. Try to quantify error.
- How to improve matching
- How much does rotation and rebinning of data change it
- How good is the matching of the datasets
- How to improve it
- How to do the final step

#### 5.1.1 Step 1

It is difficult to quantitatively determine how good the matching of the EDX dataset in the SPED dataset is, and there are many factors that contribute to the inaccuracy of the matching. Because the rotation angle was only changed by 0.4% when being iterated over, it appears that the rotation angle is not a big source of inaccuracy. A bigger potential problem is the apparent discrepancy in scaling the EDX and SPED datasets. This could be due

to the scaling factors being wrong, but can also be purely because of the preprocessing steps before image matching was performed.

As seen in Figs. 4.7 and 4.8 (and even clearer in Figs. 4.5 and 4.6 for the untreated sample), there is an overlapping region of approximately 2 nm between layers of different composition. In this overlapping region, the EDX dataset will show Ga and As peaks, although not as high as in the nanowire, and this overlap region will therefore appear bright in the EDX image. In the SPED dataset there is also an overlapping region in which the diffraction spots from the nanowire gradually lose intensity, which was measured (using HyperSpyUI) to be approximately 10 nm. This difference of lengths of the overlapping regions could cause the preprocessing steps to include slightly different regions of each datasets. As only these selected regions will appear bright in the images used for template matching, the sizes of the nanowires would be different, even though the scaling factor is correct.

However, in Figs. 4.1(a) and 4.1(b), to the right of the nanowire there is a clear difference between the EDX and SPED regions. This might also be due to the differences in overlap regions, but it gives a strong indication that the scaling factor might not be correct.

There are several possible improvements that could be made to the algorithm in order to improve these results. Firstly, a stronger filter could be placed on the images in order to not include any part of the overlap region from either dataset. Secondly, different elements in the sample, not just the GaAs in the nanowire, could be used to make the images more similar. For instance, if there are regions that have consistent diffraction patterns and compositions, these could be given a different color in the images. In this way, up to three different parts of the sample (one for each independent color) could be used to match the images together.

Improvements could possibly also have been made to the experimental setup. The current matching was possible due to the nanowire being a recognizable feature in the sample; however, the diffuseness of the edges appears to decrease the accuracy. It is difficult to change this behavior of the edges, but introducing a new feature with sharper edges might reduce the number of error sources. In addition, the accuracy of the scaling factors ought to be investigated and, if necessary, corrected to give the right values.

In the final product, the SPED dataset has been rotated and the EDX dataset

re-binned. These procedures might also introduce new errors that the person analyzing the datasets must be aware of. The rotation algorithm, though it is still in a preliminary stage and might contain errors, does not change any of the information in the datasets and should therefore be regarded as safe. The re-binning algorithm, on the other hand, can change the EDX spectrum significantly, and especially if the dataset is re-binned by a factor much larger or much smaller than unity. This is especially important to keep in mind for the smaller datasets, that have a much higher resolution than the SPED dataset, and would therefore need to be down-sampled by a large factor, resulting in a loss of information. If the purpose of the analysis is merely to qualitatively look at the composition and structure of a region in the sample, this information loss might be acceptable. However, for accurate quantitative results, one must be very careful to blindly trust the data.

## Step 2

The matching of all the datasets in the HAADF overview image gave a good result for most of the datasets. The results have been verified by eye, and so there might be errors and inaccuracies that are not easily seen. For the purpose of knowing where in the sample the different datasets have been taken from, visual confirmation of the accuracy is good enough. However, if these locations are to be used to cut out portions of the SPED dataset in order to compare it to the EDX datasets, small discrepancies might lead to wrong conclusions about compositions and structures.

The datasets that were not correctly located in the overview image, or were not part of it, gave matching values that were 20-60% lower than the datasets assumed to be the best match. This distinction is very clear in the untreated image (see Fig. 4.2(b)), but dataset A in the heated image (see Fig. 4.3(b)) gave a rather high relative matching value, even though the dataset is not part of the image. This could easily lead to false conclusions about the location of the dataset, especially if it is not immediately clear from visual inspection that the algorithm's answer is wrong.

This problem is believed to be improved by changing the way the ideal contrast level is determined. Instead of finding the overall best contrast level for all the datasets, this level can be determined for each dataset individually. This improvement is believed to simultaneously increase the accuracy of the

actual matching and increase the accuracy in which datasets that are not included in the overview image are identified as such.

Even though improving the algorithm is believed to give considerably better results, there are also changes that could and should be made to the data acquisition at the microscope. The algorithm was able to give accurate results for most of the datasets because the survey images were large enough to be uniquely identified in the overview image. However, the accuracy of the location of dataset F in the untreated sample was impossible to verify due to the survey image being too small and not containing enough distinct features. The TEM operator should therefore remember to always make sure the survey images are taken over large enough areas, or over areas which includes clear distinguishable features.

### Step 3

The final step in the procedure would be to use the locations of these EDX datasets to find the equivalent positions in the SPED dataset. This was done successfully for only one of the datasets (dataset F) - the rest resulted in mismatching array dimensions between the rotated SPED dataset and the re-binned EDX dataset. This is believed to be due to the small size (low number of pixels) of the other datasets, as datasets C and F are much larger than the rest. As already discussed, the high resolution of these remaining datasets compared to the SPED dataset might lead one to conclude that this final step is unnecessary, especially if accurate quantitative results are required.

## 5.2 Determination of $\zeta$ -values

When calculating the  $\zeta$ -factors, there are two main uncertainties: The thickness of the sample and the background subtraction. In his thesis, Garmanzlund estimates a relative error in the thickness of 5.26%. The errors due to the background subtraction are more difficult to quantify. Errors due to the background windows are believed to be lower for the peaks at higher energies due to the flatter background, as seen in Fig. 3.1.

Other uncertainties: Probe current, integration window, ...?

The spread in  $\zeta$ -values between the different regions in the samples are not significant, and are well within the uncertainty of the thickness, except for Ga and As. The large deviance between the  $\zeta$ -values for these elements between the untreated and heat-treated samples can have been caused by several different factors. Shadowing, probe currents, sample thickness

The  $\zeta$ -factors were compared to the  $k$  in order to partially verify the values. As the  $k$ -factors are known to be less accurate than the calculated  $\zeta$ -factors, the results in Fig. 4.4 are good for the lighter elements. However, the results for Pd and especially Au show very high differences between the two methods. It is again difficult to explain what the cause of this is. ???

How to make them better: Verifying by thickness??

### 5.3 Quantification

The quantification of the untreated sample gave good results in both regions. The inclusion of absorption correction gave only very minor differences in compositions, but that is to be expected when the compositions are this well-defined. The fact that the  $\zeta$ -method gave results that matched the known compositions better than the CL-method did is an indication of the validity of this method, but not a validation. Furthermore, both methods produced clearly wrong peaks, ...

The quantification of the heat-treated sample has not given as clear results as one might have hoped, and it is important to keep in mind the quantification process and not just blindly trust the presented data. For instance, the transition regions between the three layers in areas D and E are calculated to contain up to 10% Au even though none of the three layers shows more than 2% Au. The small presence of Au in the results is likely to occur due to spurious X-rays that are scattered to high angles and then produce characteristic X-rays from Au-atoms at other locations in the sample. This hypothesis is strengthened by looking at the EDX spectrum from the nanowire in the heat-treated sample, in which there is a small  $Au_{M\alpha}$ -peak (as well as a small  $Pd_{L\alpha}$ -peak). However, there is no peak of significant height to be seen for the  $Au_{L\alpha}$ -line, which lies at a much higher energy than the  $Au_{M\alpha}$ -line. +++

Why the quantification shows more Au in the transition regions than in the main layers is unknown (++discuss this), but the conclusion is nevertheless that there is likely very little or no Au in either of the layers. The accuracy of this conclusion is likely to have been verified by using the  $Au_{L\alpha}$ -line instead, as the higher energy makes it less likely to give counts because of spurious X-rays, but the high overlap with  $Ge_{K\alpha}$  makes this difficult to do in practice.

If one is to conclude that there is no Au in areas D and E, the reported amount of Pd must also be adjusted. As mentioned, the nanowire showed a small  $Pd_{L\alpha}$ -peak as well, at an energy close to that of  $Au_{M\alpha}$ , likely also a product of spurious X-rays. This will have increased the reported amount of Pd also in the Pd-rich regions, and skewed the ratios in favor of Pd. In order to estimate how much higher the reported amounts of Pd are compared to the actual amounts, one can look at the amount of Pd detected in the nanowire, that is, the inner regions of areas D and E. If the nanowire is assumed to consist of only Ga and As (or verified to do so from the diffraction patterns), there should be no Pd detected. As presented in Tables 4.2 and 4.3, the  $\zeta$ -method gave 0-7% and 0-10% Pd in the nanowire in areas D and E, respectively. Subtracting an amount of up to these values from the Pd-composition and attributing it to the other elements might therefore give a more accurate idea of the actual composition of the material. However, the nanowire also shows a composition of 0-5 and 0-7 % Ge in areas D and E, which was assumed to not be due to spurious X-rays because of the higher energy of the  $Ge_{K\alpha}$ -peak. If this result is due to spurious X-rays as well, the subtraction of Pd must be reduced accordingly, and the composition will therefore not change much.

Tables 4.2 and 4.3 gives three different results for the Pd-composition in these areas, and it is not obvious which is to be trusted to be the most correct. As discussed above, the compositions denoted  $Pd_1$  are likely to be too high due to spurious X-rays. The  $Pd_2$ -compositions calculated without  $\zeta$ -absorption give results corresponding fairly well to a subtraction of 7-10% pp Pd. However, it must be noted that if one assumes no Au in either regions, the up to 10% reported Au must be allocated to the other elements, making the  $Pd_2$ -composition slightly higher than the results in the tables, both with and without absorption correction. These results give no answer to whether the absorption correction gives more accurate results for these areas, nor to which peaks ought to be used when

The areas 1,2 and 3 in Fig. 4.9 showed similar results as for areas D and

E, and should therefore be analyzed in the same way. In Fig. 4.9(b), one may therefore assume that the Ge:Pd-ratio in areas 1 and 2 ought to be skewed from about 43:57 (for the *zeta*-method) to about 50:50, and likewise in area 3, except that also the Ga- and As-compositions should increase. This hypothesis is strengthened by looking at Fig. 4.9(c) for areas and 1 and 2, which contain no Ga or As, as Fig. 4.9(b) shows. For these regions, the results therefore ought to be accurate also for Ge, despite the overlap between peaks. It is now interesting to note the big differences caused by the inclusion of absorption correction to the  $\zeta$ -method. Without absorption correction, the results are very similar as the ones in Fig. 4.9(b), but absorption correction gives results that match very well the hypothesis of spurious X-rays giving a higher Pd-composition. If this hypothesis can be proven to be correct through analysis of the diffraction patterns, it gives a strong reason for why absorption correction can be necessary to get accurate results.

## 5.4 Comparison to theory

From the literature, [17] (++++) this part should reference introduction instead) there are some candidate compositions that one would expect to see also for this sample. Figure ?? shows the expected compositions in different layers (++++) experiment conditions). From this, one might expect to find PdGe in areas 1 and 2 in Figs. 4.7 and 4.8, GaAs with diffused Ge in the inner regions of areas D and E (??), and perhaps the expected intermediate phase Pd<sub>4</sub>GaAs in other areas.

In areas 1 and 2, the  $\zeta$ -method with absorption correction when using the Ge<sub>L $\alpha$</sub> -peak corresponds very well to the theory, and as discussed, a similar result as when using the Ge<sub>K $\alpha$</sub> -peak if the reported Ge:Pd-ratio is skewed as a result of spurious X-rays. This hypothesis is further strengthened if the inner region of the nanowire does consist of GaAs with diffused Ge, as this result would indicate that the reported presence of Ge is not just a result of spurious X-rays, in turn validating the skewing of the Ge:Pd-ratio.

For the lower and upper regions in areas D and E, the results are not as easily interpreted because the results from using the Ge<sub>L $\alpha$</sub> -line can not be trusted. The lower regions appear to consist of Ge and Pd in a ratio Pd:Ge between 3:2 and 5:3, along with traces of Ga and As in a ratio between and

1:20 and 1:5 to Pd. However, if analysis of the diffraction patterns from areas 1 and 2 reports the phase to be GePd, the same logic as above ought to be used here as well, and the Pd:Ge ratio should be skewed to between 1:1 and 5:4, depending on how much of the reported Pd and Au is attributed to each of the other elements. This would also mean that the ratios of Ga and As to Pd should increase slightly. In the upper regions the composition is Pd:Ga:As:Ge in a ratio Pd:GaAs:Ge:Au approximately between 22:4:2:1 and 12:4:2:1. Again, skewing the ratio and attributing the Au-composition to the other elements will make the expected intermediate phase  $Pd_4GaAs$  a possibility, except for the presence of Ge.

# Appendix A

## Acronyms

**FTA** Fault tree analysis

**MTTF** Mean time to failure

**RAMS** Reliability, availability, maintainability, and safety

# **Appendix B**

## **Additional Information**

This is an example of an Appendix. You can write an Appendix in the same way as a chapter, with sections, subsections, and so on.

### **B.1 Introduction**

#### **B.1.1 More Details**